Earth and Planetary Science Letters 591 (2022) 117639

Contents lists available at ScienceDirect

Earth and Planetary Science Letters

www.elsevier.com/locate/epsl

Frontiers paper

IMS observations of infrasound and acoustic-gravity waves produced by the January 2022 volcanic eruption of Hunga, Tonga: A global analysis

J. Vergoz [a,*], P. Hupe [b], C. Listowski [a], A. Le Pichon [a], M.A. Garcés [c], E. Marchetti [d], P. Labazuy [e], L. Ceranna [b], C. Pilger [b], P. Gaebler [b], S.P. Näsholm [f,g], Q. Brissaud [f], P. Poli [h], N. Shapiro [h], R. De Negri [i], P. Mialle [j]

[a] CEA, DAM, DIF, F-91297 Arpajon, France
[b] BGR, B4.3, D-30655 Hannover, Germany
[c] ISLA, HIGP, SOEST, University of Hawaii at Manoa, Honolulu, HI, United States of America
[d] Department of Earth Sciences, University of Firenze, 50121, Firenze, Italy
[e] CNRS, IRD, OPGC, Laboratoire Magmas et Volcans, Université Clermont Auvergne, F-63000, France
[f] NORSAR, Kjeller, Norway
[g] Department of Informatics, University of Oslo, Oslo, Norway
[h] Institut de Sciences de la Terre, Université Grenoble Alpes, CNRS (UMR5275), Grenoble, France
[i] Department of Earth Science, University of California, Santa Barbara, CA, United States of America
[j] CTBTO (Comprehensive Nuclear-Test-Ban Treaty Organization), 1400 Vienna, Austria

ARTICLE INFO

Article history:
Received 22 March 2022
Received in revised form 19 May 2022
Accepted 22 May 2022
Available online 3 June 2022
Editor: C.M. Petrone

Dataset link: https://www.ctbto.org/specials/vdec/

Dataset link: http://www.iris.edu

Dataset link: www.ecmwf.int/en/forecasts/accessing-forecasts

Dataset link: https://doi.org/10.31905/D808B830

Keywords:
Hunga Tonga volcano
infrasound
Lamb wave
acoustic-gravity wave
International Monitoring System
yield estimate

ABSTRACT

The 15 January 2022 Hunga, Tonga, volcano's explosive eruption produced the most powerful blast recorded in the last century, with an estimated equivalent TNT yield of 100–200 megatons. The blast energy was propagated through the atmosphere as various wave types. The most prominent wave was a long-period (>2000 s) surface-guided Lamb wave with energy comparable to that of the 1883 Krakatoa Lamb wave; both were clearly observed by pressure sensors (barometers) worldwide. Internal gravity, acoustic-gravity, and infrasound waves were captured in great detail by the entire infrasound component of the International Monitoring System (IMS). For instance, infrasound waves (<300 s period) were seen to circumnavigate Earth up to eight times. Atmospheric waves captured by the IMS infrasound network and selected barometers near the source provide insight on Earth's impulse response at planetary scales.

1. Introduction

The Hunga Tonga-Hunga Ha'apai volcano (hereafter referred to as Hunga) is a largely submerged volcano in the Tonga-Kermadec volcanic arc that formed by the westward subduction of the Pacific plate below the Indo-Australian plate. The volcanic cone rises from a depth of approximately 2,000 m below sea level and culminates with a summit caldera measuring 4 km times 2 km and reaching a mean depth of 150 m (Cronin et al., 2017). The caldera reaches the surface into the uninhabited islands of Hunga Tonga and Hunga Ha'apai, approximately 65 km north from the Tonga capital city.

* Corresponding author.
E-mail address: julien.vergoz@cea.fr (J. Vergoz).

https://doi.org/10.1016/j.epsl.2022.117639

The activity of this volcano remained mostly undetected before the Surtseyan eruptions that occurred in 2009 (Vaughan and Webley, 2010) and 2014 (Cronin et al., 2017). Based on estimates from satellite observations, the 2009 eruption drove ash plumes up to altitudes of 7.6 km and released a total amount of 0.0176 km^3 erupted material, resulting into a Volcanic Explosivity Index (VEI) 2 eruption (Vaughan and Webley, 2010). The 2014–2015 activity lasted for five weeks and was characterized by eruptive clouds rich in gas, reaching altitudes up to 10 km (Global Volcanism Program, 2022). Each of these eruptions caused an increase of emerged material and formation of new land, rapidly eroding afterwards. Samples collected on nearby islands provided evidence of highly explosive deposits dating approximately 1000 yr ago, suggesting that the collapse of Hunga volcano that generated the existing caldera might have driven the 1108 CE tropical eruption that produced more than 1 °C global cooling (Sigl et al., 2015).

After weeks of mildly sustained volcanic activity, Hunga entered a strong eruptive phase reaching a climax on 15 January 2022 at around 04:15 UTC. The rapidly rising ash cloud reached an altitude of 58 km while developing an umbrella cloud around 30 km altitude, as reported by NASA (National Aeronautics and Space Administration) Earth Observatory (Image of the Day for 17 February 2022). Within 2 h from the onset, it spread to a 600 km diameter before being distorted from the wind, indicating a large eruptive potential (Global Volcanism Program, 2022). The event was globally recorded on seismic stations as a long-lasting (∼6000 s) wave train of long-period seismic surface waves (Poli and Shapiro, 2022). From the explosive source impulse derived from globally detected surface waves, Poli and Shapiro (2022) estimated a downward vertical force ∼2.5 larger than that of the 1980 Mt. St. Helens eruption, even though more complex models might better capture the force evolution for eruptions. The corresponding VEI is 5.8, ranking the Hunga eruption among the most energetic events recorded during the last century. The explosive eruption excited different atmospheric wave modes (infrasound, Lamb, and internal gravity waves) spanning from ∼1 h period until audible, propagating at global ranges and reaching the upper atmosphere layers (Matoza et al., 2022). The large-amplitude Lamb waves generated forerunner tsunamis propagating at ∼310 m/s, which were measured worldwide – even in the Atlantic and the Mediterranean – and preceded the tsunami generated at the source in the Pacific region (Andrews, 2022). The interaction of atmospheric Lamb and gravity waves with the tsunami wave resulted in a longer-lasting tsunami than the earthquake-induced counterparts (Andrews, 2022).

Atmospheric waves were recorded by various observation networks, including the infrasound, seismic, and hydroacoustic stations of the International Monitoring System (IMS). The Comprehensive Nuclear-Test-Ban Treaty Organization (CTBTO) has been operating the IMS for 25 yr (Mialle et al., 2019). The IMS comprises four sensor technologies: seismic, hydroacoustic, infrasound (SHI), and radionuclides. The purpose of this network is to detect, identify, and locate nuclear explosions which would detonate underground, underwater, or in the atmosphere. Upon completion, the IMS will consist of 321 stations, of which 60 infrasound stations will monitor the atmosphere. Events other than nuclear explosions generating strong infrasound signals can be either of anthropogenic origin, like accidental explosions (e.g., Vergoz et al., 2019) and rocket launches (e.g., Pilger et al., 2021), or of natural origin other than volcanoes, like meteoroid events (e.g., Le Pichon et al., 2013). According to the Reviewed Event Bulletin (REB) released by CTBTO's International Data Center (IDC), all 53 IMS infrasound stations operational at the time of the Hunga explosive eruption recorded signals from the event, alongside 4 hydroacoustic hydrophone triplets and over 20 seismic IMS stations, making this the largest event ever recorded by the IMS infrasound stations and surpassing the Chelyabinsk 2013 airburst (e.g., Le Pichon et al., 2013).

Lamb waves induced by nuclear tests in the atmosphere were extensively used to estimate their yield (Pierce and Posey, 1971) in TNT (TriNitroToluene) equivalent, where 1 kiloton TNT = 4.184 $\times$ 10^{12} Joule. Such an approach has also been used to infer major explosive eruption yield, leading to 35 megatons (MT) TNT equivalent for the 1980 Mt. St. Helens eruption (Donn and Balachandran, 1981) and 70 MT for the 1991 Pinatubo eruption (Tahira et al., 1991). A maximum yield of 100–150 MT was estimated for the 1883 Krakatoa eruption (Harkrider and Press, 1967), far larger than the maximum yield of ever detonated nuclear tests (50 MT; Stevens et al., 2002).

This paper provides a comprehensive description of the chronology of the Hunga eruption as observed by the IMS technologies. The IMS infrasound network and different atmospheric wave modes are introduced in Section 2. Section 3 describes the infrasound data processing and introduces the applied methods for estimating the Hunga eruption yield. The infrasonic and acoustic-gravity waves observed across the entire IMS infrasound network as well as the unique features of the global atmospheric wave observations are described in Section 4. Potentially limiting aspects of the yield estimate and a comparison of Hunga volcano with historical eruptions are discussed in Section 5.

2. Global observations of atmospheric waves

2.1. IMS infrasound network

The entire IMS infrasound network, currently consisting of 53 certified stations, detected the Hunga explosive eruption. Besides infrasound, these stations also enabled global observations of Lamb waves. Fig. 1 shows the station locations and the modeled arrival times of both wave types using celerities estimated from the atmospheric conditions (see Supporting Information SI1). The nomenclature used for the identification of the different wave passages follows Matoza et al. (2022): A1 for the direct short-orthodrome arrival, A2 for the first long-orthodrome arrival, A3 for A1 plus one circumnavigation, etc.

The IMS infrasound stations are arrays of at least four sensors with apertures ranging from 1 to 4 km. All sensors are equipped with wind-noise reduction systems for reducing small-scale disturbances at a sensor. Indeed, infrasound monitoring capability is limited by local wind conditions, particularly related to atmospheric convective turbulence. In the 0.01–0.5 Hz band, infrasound noise generally increases with wind speed by ∼5 dB per m/s (Walker and Hedlin, 2010). Installed sensors are microbarometers, sensitive to pressure changes down to 1 mPa. IMS stations continuously sample the differential pressure (BDF channel) at a rate of 20 Hz. The instrument response of this channel is designed for the frequency range ∼0.01–5 Hz. At lower frequencies, BDF amplitudes are recovered by deconvolution to correct the high-passed pressure data for the instrument responses as referenced in the IDC databases. This restitution is performed in the frequency domain using a sensor-dependent waterlevel corresponding to the minimum frequency of 0.1 mHz, as implemented in ObsPy (Beyreuther et al., 2010).

2.2. Atmospheric waves

The Navier-Stokes equations for compressible flow in the presence of gravity govern the mechanical wave motion types discussed in this paper, known as acoustic-gravity waves (AGW). Their study invariably relies on the linearized, small-amplitude perturbation expansion of the equations (e.g., Gossard and Hooke, 1975).

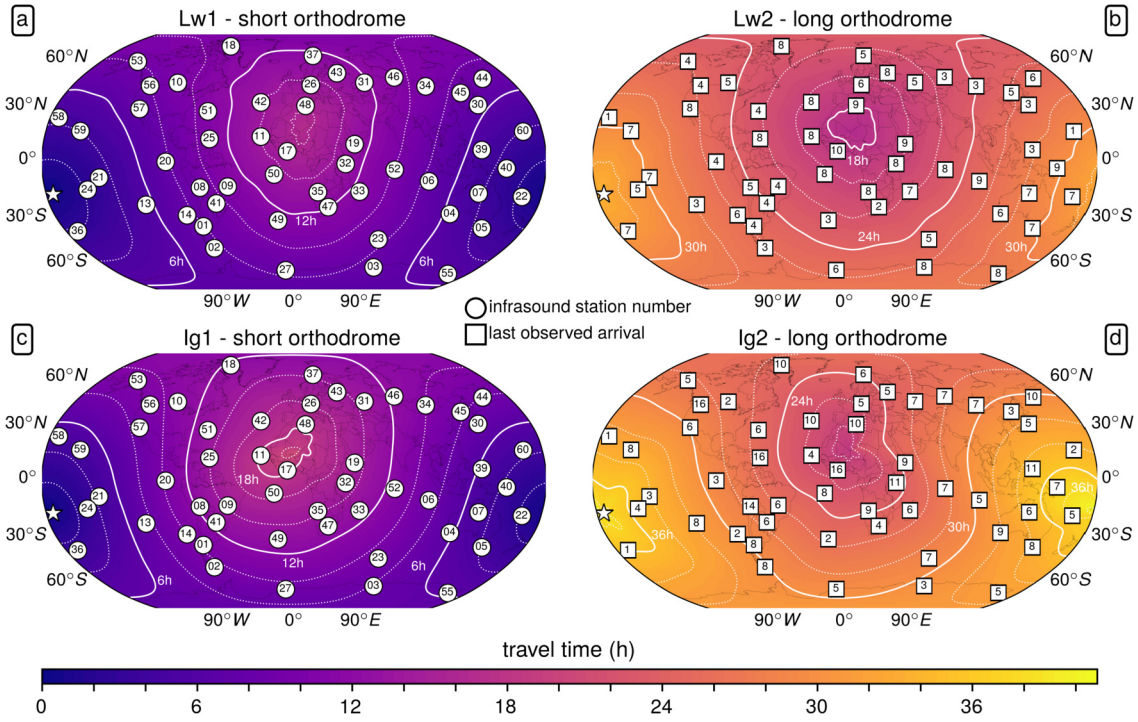

Fig. 1. Station maps of the 53 certified IMS arrays; the estimated short-orthodrome (a, c) and long-orthodrome (b, d) propagation times of Lamb waves (a, b) and infrasound waves (c, d) from Hunga are color-coded and depicted by isochrones each 2 h. The infrasound network station numbers are indicated by circles (a, c). For each wave type and array, the last observed arrival (see Section 3.1) is indicated by a number (denoting A1 to A16) in the square (b, d).

Four types of modal solutions emerge: acoustic waves, acoustic-gravity waves, internal gravity (buoyancy) waves, and the special surface-guided Lamb waves.

While gravity and compressibility terms of the governing equations are important for acoustic-gravity modes, compressibility dominates for frequencies higher than the buoyancy or Brunt-Väisälä (BV) frequency around 3.3 mHz, and AGW reduce to infrasonic waves. Since the acoustic cutoff and BV frequency change with elevation (Gossard and Hooke, 1975), an acoustic-gravity mode in the troposphere may turn into an acoustic mode in the thermosphere (Kshevetskii et al., 2021). Therefore, the association of wave types is ambiguous around the BV frequency.

The soliton-like wave which traveled around the Earth corresponds to the Lamb wave solution (e.g., Lamb, 1932). It emerges from the governing AGW equations when the vertical velocity is set to zero. The energy is theoretically confined within the lower scale height (∼8 km) of the atmosphere, whereas it concentrates at larger atmospheric scales for other acoustic and gravity modes (Francis, 1973). Its nominal group velocity is ∼310 m/s (e.g., Press and Harkrider, 1962; Bretherton, 1969) where this value depends on the lower atmosphere effective sound speed, explaining the asymmetric travel time isochrones in Fig. 1. Under ideal conditions the Lamb wave propagates as an edge wave (Pierce and Posey, 1971) above a horizontal boundary in a windless isothermal atmosphere (Bretherton, 1969). Although Earth's atmosphere is neither isothermal nor restless, Lamb waves can be observed after highly energetic events as well as in the ambient pressure field (Nishida et al., 2014). Surface friction can limit Lamb wave lifetimes, which are of the order of days (Lindzen and Blake, 1972); their attenuation distance largely exceeds the ∼40,000 km circumference of the Earth – far beyond acoustic-gravity modes' (Francis, 1973). Lamb waves bridge the gap between acoustic and acoustic-gravity modes since they can exist at all periods between a few minutes to less than a day (Francis, 1973).

Fig. 2 illustrates the different modes discussed above using Stockwell-transform (Stockwell et al., 1996) spectrograms derived from observations at the closest IMS station IS22 in New Caledonia (1,847 km from Hunga) and the more distant IS32 in Kenya (15,752 km). IS22 simultaneously recorded the Lamb mode arrival in the 100–5000 s bandpass and acoustic modes in the 2–100 s band while the arrival sequence at IS32 emphasizes the arrival time differences due to the larger Lamb wave celerity (nominally 310 m/s) compared to that of stratospheric and thermospheric infrasound arrivals (typically 220–270 and 270–320 m/s, respectively). The actual arrival times coincide with the estimated travel times shown in Fig. 1. Internal gravity wave modes, which have lower celerities (typically <50 m/s), reach IS22 later, around 08:00 UTC (see energy between 1000 and 250 s at IS22). An interesting feature in the acoustic regime is the double dispersion line observed at IS32 (Fig. 2b) during the A1 arrival (∼18:00–21:00 UTC). The lower one (from 200 to 50 s) corresponds to wavelengths consistent with the thermospheric waveguide and is observed on more than half of the IMS infrasound stations. It is also observed during the A2 arrival (long orthodrome) on the next day (∼02:00–05:00 UTC). The upper dispersion line (50 to 25 s) is clearly visible for A1 on 14 stations, all located west of the volcano (in Australia, the Indian Ocean, and Africa). It corresponds to wavelengths consistent with the stratospheric waveguide. IS32 is the most remote station for which the stratospheric waveguide is strong and steady over the entire source-receiver path.

Such dispersive propagation effects are often observed from much shallower waveguides which can interact with infrasound waves generated by much smaller energy events (Vergoz et al., 2019). This simultaneous evidence of dispersion lines associated to both stratospheric and thermospheric ducts is unique. Dispersion of internal gravity modes is also observed at IS22 (Fig. 2a), between 07:00 and 14:00 UTC with a sweep from 500 to 200 s. These time-frequency behaviors are in general agreement with dispersion curves derived in the literature (Press and Harkrider, 1962; Pierce and Posey, 1971), the lower frequencies corresponding to acoustic-gravity modes and the higher to acoustic modes. These observations spanning the acoustic-gravity to acoustic frequency

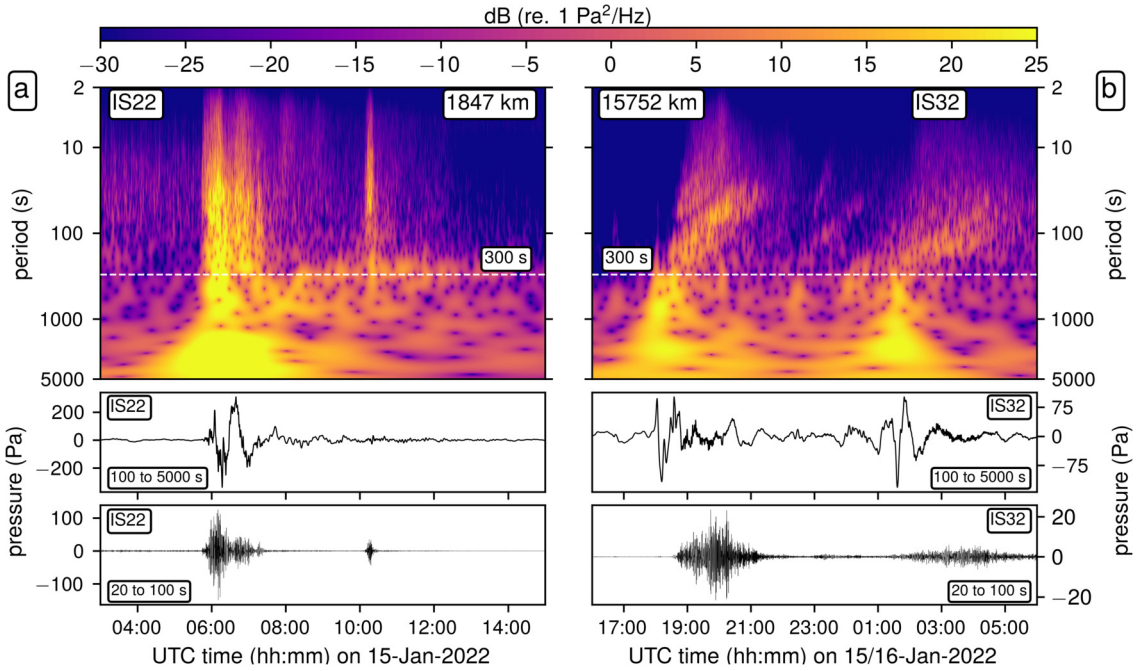

Fig. 2. Stockwell-transform spectrograms of (a) IS22 (New Caledonia, 1,847 km from Hunga) over 12 h and (b) IS32 (Kenya, 15,752 km) over 14 h. The horizontal dashed line recalls the approximate value of the Brunt-Väisälä (BV) frequency in the lower troposphere (∼300 s). Two different bandpass filters are applied to the instrument-corrected waveforms to visualize the low-frequency infrasound (20–100 s, bottom) and acoustic-gravity and gravity wave modes (100–5000 s, middle). At IS32, both the first short-orthodrome (A1) and the first long-orthodrome (A2) arrivals are separated by ∼8 h. The dispersion line above 300 s flattens with the A2 arrival.

range will require further investigation to fully explain the various patterns visible in the spectrograms by mode transitions.

3. Methods

3.1. IMS infrasound data: processing and detections

For processing the infrasound records and to characterize coherent wavefront properties, the progressive multi-channel correlation method (PMCC; Cansi, 1995) is applied to the BDF data of IMS arrays. This method, implemented at the IDC (Mialle et al., 2019), estimates arrival parameters based on inter-element cross-correlation and time delays. The PMCC processing time window and frequency band configuration is using 1/3-octave band standardization in the 0.01 to 4.0 Hz frequency band and implemented by Hupe et al. (2022) to process the historical IMS dataset. Window lengths are linearly scaled to the period, with 90% overlap. Such configuration improves the station detection capability while allowing better discrimination between interfering signals in a wide frequency band. For a detailed wavefront property analysis, the configuration setting of the time-frequency bands has been extended to cover the acoustic-gravity and acoustic range (0.002–1 Hz) using the instrument-corrected waveforms. The calculated wave parameters include the backazimuth, the frequency, the root-mean-square amplitude, and the apparent velocity. PMCC has proved to be efficient for detecting coherent low-amplitude acoustic waves within incoherent noise as it only requires a single computational run for the frequency range of interest (e.g., Vergoz et al., 2019; Hupe et al., 2022).

Since the IMS infrasound frequency range of interest lies between 0.02 and 4 Hz, lower frequency observations have to be treated with caution. The instrument-corrected BDF data lead to realistic amplitude recovery down to 0.1 mHz for most of the infrasound sensors established throughout the IMS. Marty et al. (2021) show that updated high/low noise models could be established with a good confidence down to ∼0.01 mHz. This is confirmed by the generally good agreement between the recovered Hunga Lamb waves obtained from the instrument-corrected infrasound data and the barometric static pressure data, which exist at each IMS infrasound station. For Hyperion IFS sensors, however, the barograms and unexpectedly low amplitudes indicate systematic instrument deconvolution issues (Matoza et al., 2022), likely due to missing relevant information on the nature of the sensors and a sharper transition than other microbarometers in the response function under 0.01 Hz. Moreover, the wind-noise reduction systems of the infrasound stations are most efficient above 0.5 Hz. Depending on the local conditions, wind noise can affect measurements and low frequencies (Section 2.1).

Low frequencies correspond to wavelengths much larger than the array apertures (1–4 km), which potentially biases coherent wave detection within the background noise. Nevertheless, PMCC detections resulting from the adapted processing down to 2 mHz coincide well with the spectral content of the waveforms and notably resolve the transition between acoustic, acoustic-gravity, and internal gravity wave modes (cf. Fig. 2).

Based on the estimated arrival times and the theoretical backazimuths, the last infrasound arrivals associated with the eruption are identified using the PMCC detections, as denoted per station in Fig. 1d. Since the dominant periods of the observed Lamb waves range between 30 and 50 min (e.g., Fig. 2), these are not necessarily covered by the PMCC detections. Therefore, the last Lamb wave arrivals denoted in Fig. 1b are found by inspecting the response-corrected waveforms for large-amplitude signatures in the relevant frequency band around the estimated arrival times.

3.2. Lamb waves and high-yield estimates: a delicate matter

Following the observations of Lamb modes that were emitted by atmospheric nuclear tests, Pierce and Posey (1971) – hereafter PP71 – developed a theoretical formula to estimate the yield of near-surface atmospheric nuclear explosions based on the amplitude and period of the Lamb waves. Considering a scale height value of 8 km (e.g., Lamb, 1932) and converting the original PP71 expression for bursts in the troposphere to SI units returns

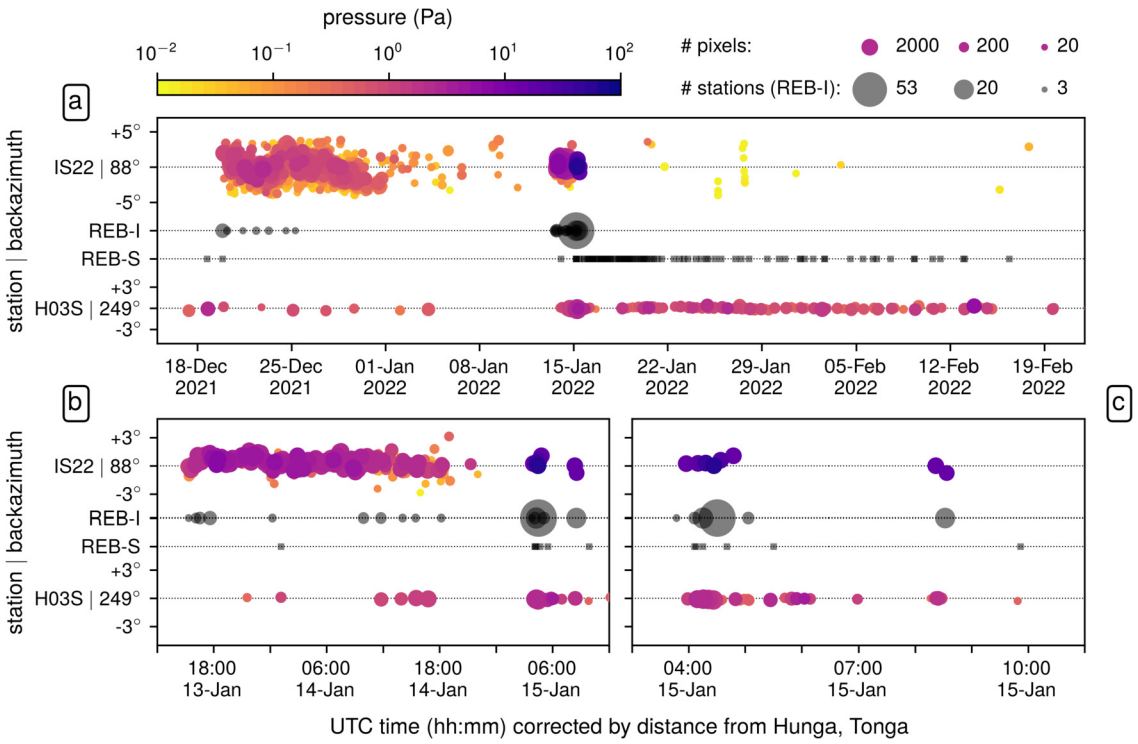

Fig. 3. SHI source chronology of Hunga volcano reflecting the December to February eruptive activity within (a) roughly 2 months, (b) 2 days, and (c) 8 hours around the 15 January 2022 eruptions of Hunga volcano (major seismic event at 04:15 UTC). The infrasound and hydroacoustic detections of IS22 (backazimuth 88°) and H03S (249°), respectively, are color-coded by the maximum peak-to-peak amplitude of coherent signal arrivals from Hunga volcano and projected back in time using celerities of 300 m/s and 1.48 km/s. Detections with larger amplitudes are stacked on top of smaller amplitude detections. The size of the color-coded circles is scaled to the number of PMCC pixels per detection (one pixel is a unitary time-frequency cell used by PMCC to build detections). Events listed in IDC's REB are aligned as semi-transparent grey markers for both seismic (squares) and infrasonic events (circles), the latter of which are sized by the number of detecting stations. Infrasound signals detected at IS22 after 15 January 2022 are likely associated to Pacific microbaroms rather than Hunga volcano, as their frequency content (around 0.2 Hz) indicates.

$$Y_{\mathrm{kt}} = 0.34 P_{\mathrm{p2p}} (T_{1,2})^{\frac{3}{2}} \sqrt{\sin\left(\frac{r}{R_E}\right)} \tag{1}$$

where Y_{kt} is the equivalent TNT yield in kilotonnes, P_{p2p} is the peak-to-trough gauge pressure (in Pa), $T_{1,2}$ is the time (in s) between the two first positive peaks of the identified Lamb waveform, r is the great circle distance from the origin to the station, and R_{E} is Earth's radius.

IMS infrasound data permits equivalent TNT yield estimates of any detectable explosive nuclear event based on scaling laws made for infrasound measurements as discussed by Green and Bowers (2010). These authors cite the Los Alamos National Laboratory relationship where stratospheric winds variability is taken into account. They also note that half of the released energy from a nuclear explosive actually forms into the blast, the rest converting to thermal and radiation energy as opposed to high explosive detonation (Garcés, 2019). Another factor of two is introduced when a source is on or near a reflective surface, in contrast to a detonation in free air (Garcés, 2019). These are crucial impacts for equivalent TNT yield estimates. Similar care should be taken when invoking the PP71 relationship. Its theoretical development assumes a point explosive detonation and is designed for frequencies around the BV frequency. However, this is outside the most energetic period range obtained from instrument-corrected IMS signals of the Hunga event (~2000–3000 s, Fig. 2). Therefore, Lamb modes need to be filtered at an appropriate frequency range. The PP71 equation was developed for nuclear tests and therefore for a source mechanism that differs significantly from volcanic eruptions. Since both detonations and volcanic explosions can radiate Lamb waves, the PP71 equation has been used to estimate an equivalent TNT yield of volcanic eruptions, such as for Mt. St. Helens (Donn and Balachandran, 1981) or Pinatubo (Tahira et al., 1991). This approach reduces blast signal complexity from diverse explosive types (low, high, nuclear) to a single standardized metric to compare the explosive energy of different events. Section 4.3 discusses how and at which IMS stations PP71 could be applied. Energy estimates based on revisited yield scaling laws (Schnurr et al., 2020) are fairly reliable within a stable range of scaled distances (Kim et al., 2021). This additional method brings elements of comparison to the results obtained with PP71.

4. Results

4.1. Source chronology of Hunga, Tonga, inferred from SHI records

The three IMS waveform technologies (SHI) are used to reconstruct Hunga's recent eruptive chronology, which began in mid-December 2021 (Global Volcanism Program, 2022). Fig. 3 shows relevant detections by the closest infrasound array (IS22) and a hydroacoustic station in the Pacific colocated to IS14 on Fig. 1a (H03, Juan Fernández Island, 9,350 km) along with infrasonic and seismic REB events from 15 December 2021 to 22 February 2022 (Fig. 3a). Stable austral summer stratospheric downwind conditions benefited Hunga's detection at IS22 during this period. Hunga's eruptive phase started with a significant infrasound event on 19 December 2021 at 20:46 UTC (REB time), detected by 12 infrasound arrays. Following this eruption, IS22 recorded continuing but decreasing activity until 4 January 2022, as reflected by decreasing amplitudes and number of arrivals. After a quiet period of 9 days, the infrasound activity resumed on 13 January with two stronger events detected by 4 and 11 infrasound stations (15:19 and 17:37 UTC, respectively). Compared to the December activity, the detected infrasound amplitudes were almost 10 times larger, whereas the duration of this sequence was only 2 days (Fig. 3b). While the in-

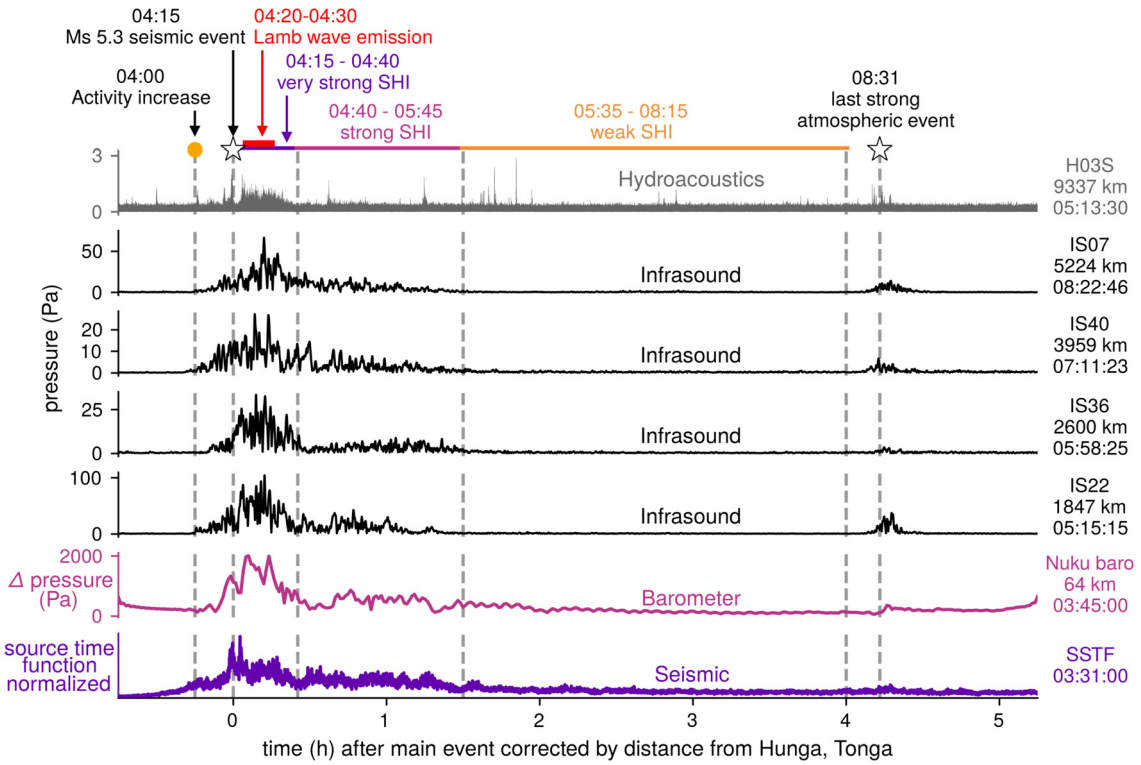

Fig. 4. Main eruptive sequence of Hunga volcano from the comparison of 6 h of the short-period SSTF component (0.01–0.03 Hz, bottom trace) with infrasound (0.02–0.05 Hz) and mean-free absolute pressure (barometer in Nukuaʻlofa, Tonga) recordings near the source. For each station, the waveforms' envelopes have been aligned relative to 45 min before the arrival times of the phases associated to the seismic event (04:15 UTC). The main atmospheric event associated to Lamb wave emission occurs between 04:20 and 04:30 UTC. The time axis at the bottom represents the corresponding retarded time. Reference times are indicated on the right under the station name. Both the SSTF and the waveforms reveal several eruptive phases, which are denoted on the timeline at the top.

frasonic intensity reduced on 14 January, the hydroacoustic activity recorded at H03 increased for 6 h. The eruptive phase climaxed on 15 January 2022 between 04:00 and 04:30 UTC, visible across all SHI observations (Fig. 3c). The strongest seismic event (REB: Ms 5.3) occurred at 04:15 UTC, whereas the strongest REB infrasound event, detected by the whole IMS infrasound network, is timed around 04:30 UTC. IS22 detections exhibited amplitudes another 10 times larger than 2 days before.

A last strong eruption detected by 25 infrasound and 3 hydroacoustic stations occurred at 08:31 UTC. This eruption concluded the infrasonic and thus subaerial activity of Hunga. In the aftermath, however, the number of seismic events and hydroacoustic H03 detections suddenly increased and exhibited a sustained but fading activity for one month. A possible interpretation – beyond classic aftershock series – is that these modest-size earthquakes (mb 4–5) detected by low-noise seismic networks and well-sited hydroacoustic stations could accommodate the collapse of the volcano (caldera forming event) that occurred within the hours following the main blast. Further investigation is needed to confirm or refute this hypothesis (see Section 5.2).

Hunga volcanic explosion generated strong seismic Rayleigh waves that were recorded by the global seismic networks. Poli and Shapiro (2022) used these signals to characterize the seismic source corresponding to the explosion as a reaction force from the volcanic jet acting on the ground (e.g., Kanamori and Given, 1982). Building upon that characterization and seismic data, a seismic source time function (SSTF) is derived in this study. For this purpose, the propagation of Rayleigh waves from the volcano is modeled using a 3D velocity model (Ekström, 2011) and attenuation from PREM (Dziewonski and Anderson, 1981). The propagation (dispersion, attenuation, and spreading) is deconvolved from vertical-component data recorded at global stations (Poli and Shapiro, 2022, and references therein) to obtain series of one-station SSTF estimates. The final SSTF that represents the displacement at the source position is computed as an average of amplitudes of all single-station estimates. As discussed by Poli and Shapiro (2022), the spectral analysis of the source process indicates two separate time scales. Fig. 4 shows the short-period component of the SSTF computed after filtering the signals between 0.01 and 0.03 Hz. After a short period of silence, the main eruptive phase initiated from 04:00 to 04:15 UTC with an increase of SHI activity and a spectacular exponential increase of atmospheric activity. At 04:15 UTC, a Ms 5.3 seismic event marked the beginning of the most intense explosions sequence, which maximized towards 04:30 and ended around 04:40 UTC. The Lamb wave was likely emitted between 04:20 and 04:30 UTC. The peak absence in the SSTF around 04:30 UTC suggests a decoupling of seismic and atmospheric sources during that sequence, but the complex generation mechanism requires further investigation. The following 4 h were characterized by rather moderate activity but with hydroacoustic peaks and ended with a final strong eruption around 08:31 UTC. The comparison of the SSTF with local and remote pressure data confirms that the selected sensors shown in Fig. 4 detected the same component of a complex source sequence associated to the main eruptive phase. For instance, the absolute pressure recordings of the barometer station in Nukuaʻlofa, Tonga's capital, highlight the long-period pressure fluctuations near the volcano and also reveal the second explosive eruption at 08:31 UTC. The SSTF also exhibits a good correlation with the infrasound observations at IS22, IS36 (New Zealand), IS40 (Papua New Guinea), and IS07 (Australia) in terms of relative amplitudes and durations within the 0.02–0.05 Hz band. These are the four closest IMS stations located under favorable and stable stratospheric downwind conditions. Therefore, for these frequencies and propagation conditions, recorded amplitudes matched at first order the generated source levels while

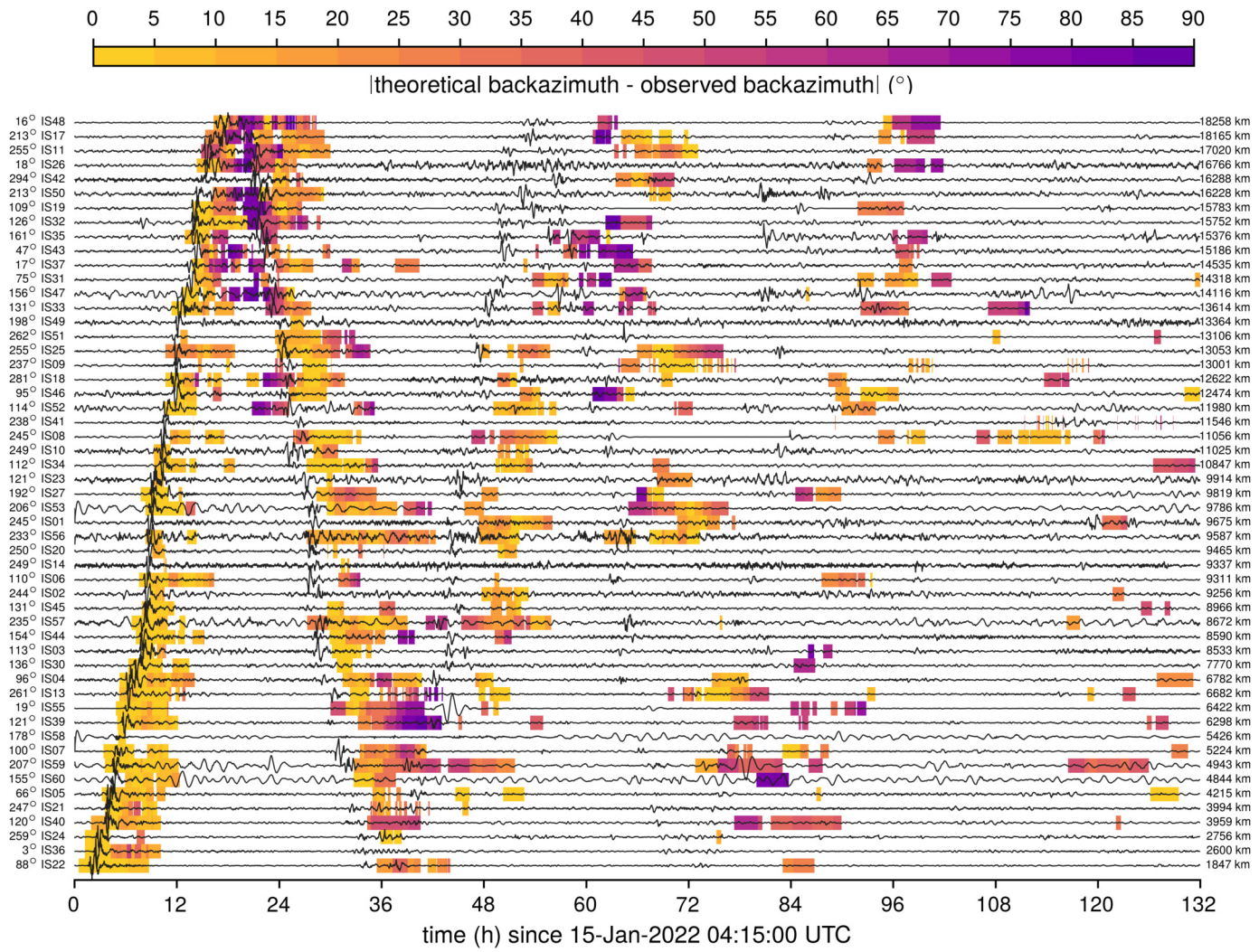

Fig. 5. Global instrument-corrected infrasound recordings sorted by distance from the source, with one sensor trace displayed per IMS station. The restituted broadband waveform traces of BDF channels are bandpass-filtered between 200 and 5000 s, dominated by large-amplitude Lamb waves. Each trace is normalized by its absolute maximum. The background coloring displays backazimuth deviation derived from PMCC low-frequency detections performed in the 1–500 s frequency band. These detections correspond to acoustic phases related to the main eruption (and partly the 08:31 event, see e.g., Figs. 2–4). While Lamb waves propagate at an almost constant celerity of around 310 m/s (depicted as a clear "M" shape on the waveforms), infrasound waves travel slower and are very sensitive to the atmosphere dynamics up to thermospheric altitudes (progressively deformed "M" shape on the detections after one global circulation). The color scale spans from the minimum observed deviation compared to the theoretical backazimuth on either the short or long orthodrome for each station.

propagation effects did not significantly impact the duration of the recorded signals.

4.2. Global characterization of infrasound and Lamb waves using broadband PMCC processing

The Hunga explosion is the first single event detected by all operational IMS infrasound stations. Fig. 5 displays instrument-corrected waveforms associated with this event for all IMS stations sorted by distance from the source within 132 h since the eruption (5.5 days). High-amplitude signals are Lamb waves characterized by periods >2000 s. Each waveform has a color-coded background representing the smallest absolute backazimuth deviation of PMCC detections calculated in the infrasound band (0.002–1 Hz, see Section 3.1) for the short-path or the long-path arrival (theoretical backazimuth ±180°). PMCC A1 (short-orthodrome) arrivals show backazimuth deviations below 5° for most of the detecting stations (50 of 53). However, the deviation increases slightly near the antipode, to which IS17 (Ivory Coast) and IS48 (Tunisia) are the closest. Between A1 and A2 (long-orthodrome) arrivals, an exceptional drift in backazimuth deviations occurs at stations within 6,000 km from the antipode (IS47 to IS48), with values up to the largest possible deviation (90°). The A2 arrivals still have relatively low deviations, although higher than A1's. The azimuthal drift repeats near the source between A2 and A3 arrivals. This global pattern can be recognized four times, even when the number of detecting stations decreases with successive arrivals. A6 is the last visible arrival in Fig. 5. Some stations did not detect A1, due to the combined effects of high local wind noise and unfavorable propagation conditions. Instead, these stations clearly detected the long-orthodrome arrival A2 (e.g., IS42, IS49) or only A3 and A4 (IS01). The Lamb waves encircled the globe once within ~36 h, with faster travel times (Fig. 1) that produced an increasingly larger time delay to the shorter period PMCC infrasound detections for longer travel paths (Fig. 5). Four full Lamb wave circulations around the globe can be confirmed with a couple of infrasound stations by a detailed inspection of the waveforms (see Fig. 1b for the last Lamb wave arrivals per station).

Fig. 6a provides a detailed half-day view of PMCC detections at IS22 (same time window as Fig. 2a). For comparison, 3 days of PMCC detections at this station, plus IS32, IS25, IS37, and IS48, are provided in SI2. The arrival times of these detections coin-

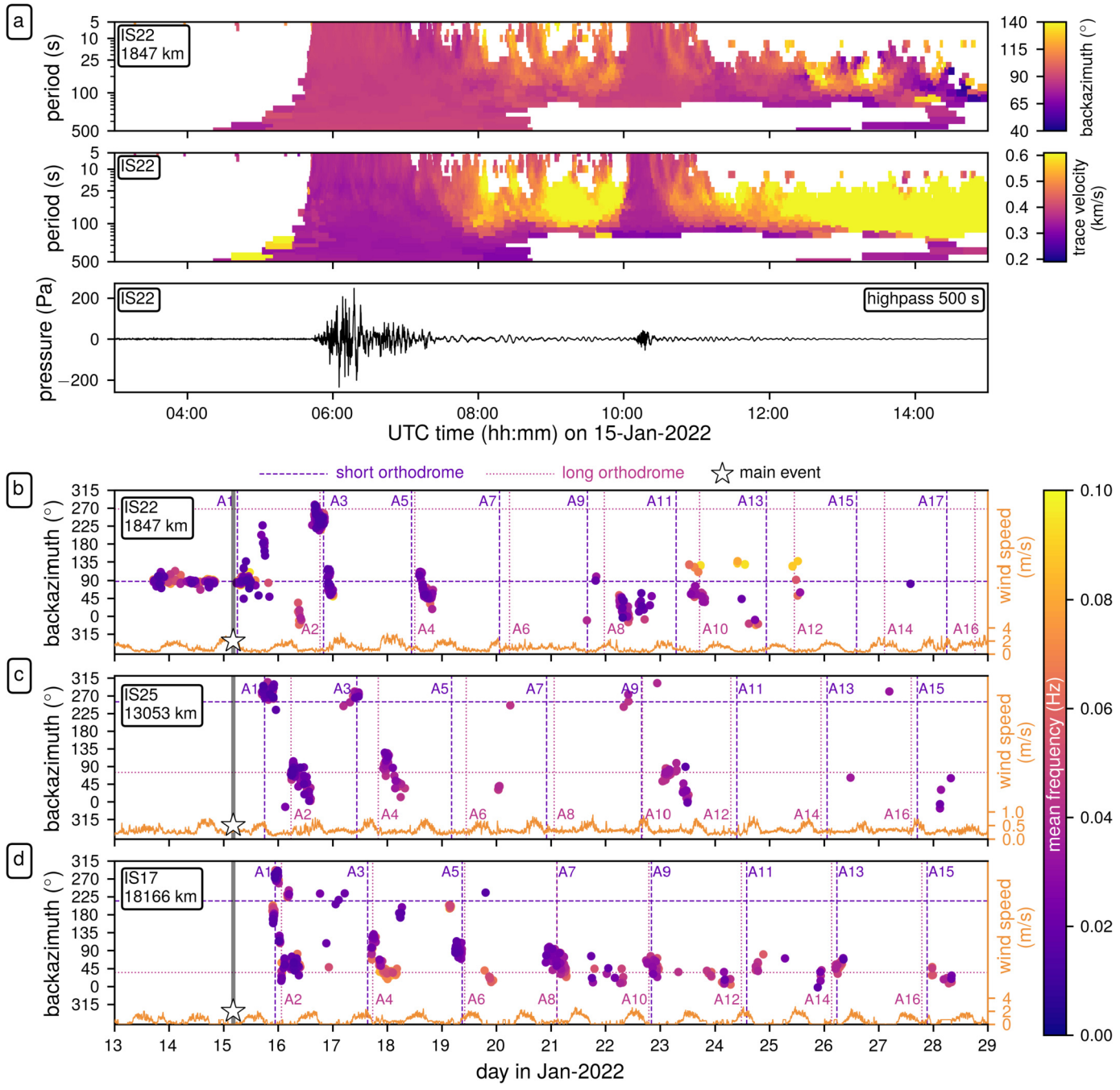

Fig. 6. (a) IS22 PMCC detection results and waveform bandpass-filtered for the PMCC frequency range, showing signals of the first (04:15 UTC) and the second eruption (08:31 UTC). (b, c, d) PMCC infrasound detections (≥0.01 Hz) of 16 days at IS22, IS25, and IS17; low-frequency arrivals around the theoretical backazimuths and arrival times are attributed to Hunga volcano. The near-surface wind speed at the station (10 min average, orange line) indicates the noise conditions that affect the detection capability (see SI2).

cide with the predicted ones obtained from ray-tracing (as shown in Fig. 1). IS22 captured also the second eruption at 08:31 UTC (Fig. 6a), which generated both Lamb and infrasound waves (cf. Fig. 2a).

Figs. 6b–d show simplified PMCC views extended to 16 days for IS22, IS25 (Guadeloupe, 13,053 km), and IS17 (Ivory Coast, 18,165 km), respectively, showing detections along with the predicted arrival times (SI1). At IS22 and IS25, the backazimuth deviation from true is increasing with the number of arrivals (e.g., from A1 to A4/A5), whereas a broad backazimuth range is instantly observed at IS17 for the first two arrivals (A1–A2). This holds for the majority of the stations within 6,000 km from the antipode (Fig. 5). From A6 onwards, long-orthodrome arrivals are dominant and adapt to the theoretically corresponding backazimuth at IS17. IS17, IS25, and IS56 are the only stations detecting A16, corresponding to long-orthodrome signals that traveled more than seven times around the globe during more than 13 days. After one global circulation, detections are visible only under low wind noise conditions (e.g., no detections at IS22 associated to A6–A7; see also SI2).

4.3. Yield estimate: using the IMS network and near-field barometers

The propagation of the Lamb waves across the IMS is illustrated in Fig. 5. Lamb wave amplitudes (P_{p2p}) and periods ($T_{1,2}$) are de-

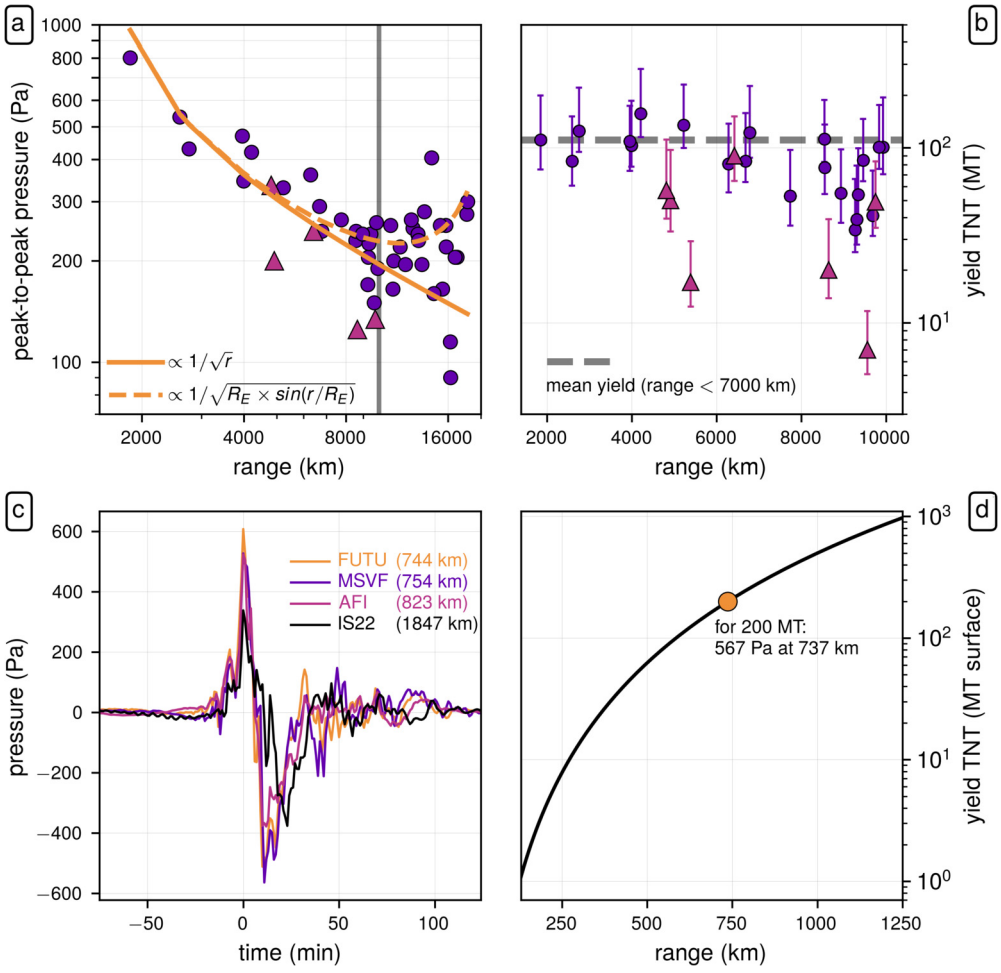

Fig. 7. Yield estimation using (a, b) PP71 model and the IMS and (c, d) barometers and scaling laws. (a) Peak-to-peak amplitudes of the Lamb wave as a function of range for IMS infrasound stations. Trends (dashed and dotted orange lines) are superimposed to guide the eye and the discussion. Reddish triangles indicate measurements from stations equipped with Hyperion IFS sensors (three stations are not displayed, due to their very low amplitude). (b) Energy estimates using PP71 model for Lamb wave signals bandpass-filtered in the 200–500 s range, with error bars. (c) Waveforms of barometers (colored) closer to Hunga than the closest IMS infrasound station IS22 (in black). Distance of each station to Hunga is shown in the legend. (d) Applying the Schnurr et al. (2020) empirical fit in the sweet spot for the closer barometers shown in (c) assuming a most probable peak value of 567 Pa at a scaled range 100 m/(kg)$^{1/3}$ for a 200 MT surface blast.

termined (see Section 3.2) from these instrument-corrected recordings. Fig. 7a shows Lamb wave P_{p2p} as a function of great-circle distance. Predicted and observed spreading of energy is cylindrical and amplitudes should decrease with $r^{-1/2}$ in the intermediate range before Earth's curvature becomes important. This trend is reported in Fig. 7a. Interestingly, the Lamb wave amplitudes remain constant or even slightly increase beyond ~10,000 km. The Earth's curvature effect, which contributes to lateral focusing of the waves, may cause this behavior as recalled in PP71. The authors used pseudo-cylindrical coordinates to highlight how the effect of Earth's curvature is accounted for – among other factors – with the geometrical term $(R_E \sin(r/R_E))^{-1/2}$ (Fig. 7a). A few stations exhibit unexpectedly low peak-to-peak amplitudes – for instance, IS47, IS56, and IS58 (4, 18, and 50 Pa, respectively). These measurements rely on Hyperion IFS sensors (triangles in Fig. 7) and are considered as outliers in this analysis (see Section 3.1), artificially lowering yield estimates.

Following PP71, where frequencies around BV (~3.3 mHz) have to be considered, Lamb wave signals were bandpass-filtered between 200 and 500 s and P_{p2p} and $T_{1,2}$ values were picked up again. The corresponding yield estimates are displayed in Fig. 7b for distances up to 10,000 km, where lateral focusing starts and for which PP71's formula is not valid anymore. Accounting for uncertainties introduced by manual picking of amplitudes and periods as well as filtering (details are provided in SI3), overall, asymmetric errors were obtained as shown in Fig. 7b. With increasing distances, yield estimates tend to decrease, possibly related to limitations of PP71's model and/or to the distortion of the filtered waveforms due to propagation effects as lateral changes in celerity and topography. Therefore, only stations up to 7,000 km away from Hunga volcano were considered and an average yield of 111 ± 23 MT was obtained.

Three stations of the global barometer sensor network are within the sweet spot for Sachs' scaling relations (Kim et al., 2021), corresponding to a scale range of 20 to 100 m/(kg)$^{1/3}$. The blast waveform characteristics have their lowest uncertainty and the highest predictability in the sweet spot. Stations in Maopo'opo, Futuna (G.FUTU.LDI), Monasavu, Fiji (II.MSVF.LDI), and Afiamalu, Samoa (IU.AFI.LDO) are at ranges of 744, 754, and 823 km from the source, respectively. The observed peak overpressures (Fig. 7c) of the instrument-corrected and low pass filtered signals (120 s cut-off) match the most likely peak overpressure of 567 Pa predicted at a range of 737 km by Schnurr et al. (2020) for an equivalent surface yield of 200 MT TNT equivalent (Fig. 7d). Scaled pressure and ranges show exceptional stability in the peak overpressure for the three nearest stations within 823 km from the source, suggesting they are representative of the source pressure function for the Lamb wave. It is important to note that this includes a coarse factor of two that accounts for a surface (200 MT) vs. free-air (400 MT) detonation assuming a perfectly reflecting boundary; the

equivalent yield may be higher from reflectivity arguments (Garcés, 2019). Multi-resolution analysis of the nearest stations returned an observed blast peak period of ∼2000 s (33 min), four times larger than the ∼500 s peak period that would be expected for a 200 MT surface detonation (Garcés, 2019). This is not surprising, as eruption processes can be characterized as slower low explosives (Garcés et al., 2013) with much longer periods than high explosives.

Both methods presented above provide yield estimates consistent with each other in order of magnitude (100–200 MT surface) and an uncertainty factor of two. This uncertainty is typical for historical yield estimates from high-explosive detonations (e.g., Garcés, 2019), and therefore is not surprising for a poorly constrained volcanic blast, which is highly complex in its nature as shown in the long-duration SSTF (Fig. 4).

5. Discussion

5.1. An exceptional backazimuth drift

The infrasound detections exhibit a significant drift in the backazimuth (up to 90°) within a single arrival at certain IMS stations (Fig. 5). This drift is most prominent within 6,000 km from the antipode and affects all infrasound passes around the globe. Several path effects may contribute to this phenomenon, including: 1) the horizontal refraction of acoustic wavefronts as they traverse one or several stratospheric polar vortices, similar to the bending effects observed at the edge of cyclonic wind fields (Blom and Waxler, 2017); 2) inhomogeneities and multiple scattering along the propagation path, causing a broadening of the sound rays (Červený and Soares, 1992), where low-frequency sound reaching the station arrives from wider regions of diffraction that in turn correspond to a wider backazimuth interval; 3) for later arrivals, the propagation of gravity waves and nonlinear acoustic waves produced during the eruption sequence can lead to long-lasting perturbations of atmospheric temperatures and velocities. These can have a striking effect on acoustic wave generation and propagation characteristics, hence inducing a highly complex and multiply scattered infrasound source in space and time.

To provide a preliminary assessment of the influence of wind and temperature variations on the backazimuth drift, ray paths were computed using 3D range-dependent ray-tracing (Blom, 2019) together with ECMWF, MSIS00 (Picone et al., 2002), and HWM14 (Drob et al., 2015) atmospheric specifications. These reveal that the ray paths are bent significantly as they traverse the Arctic stratospheric polar vortex region (Fig. 8a), compared to rays computed for a windless atmosphere (Fig. 8c). Furthermore, the drift was modeled for IS37 in Norway, which showed a large backazimuth drift in the recordings (see Fig. S3, SI2), despite being 4,000 km away from the antipode. Due to the inherent high-frequency approximation of ray-tracing and uncertainties in the considered profiles, this modeling cannot fully reproduce the observations. For estimating the backazimuth drift, the celerity and backazimuth at ground hits were extracted within 400 km from IS37 (see SI4), and the arrival time at each ground hit was corrected for the distance by considering a relative time $t_{rel} = r_{IS37}/c_i$, where r_{IS37} is the distance between Hunga and IS37, and c_i the predicted celerity for ground hit i. This yields an increasing trend in backazimuth with relative effective arrival time (Fig. 8b). Although there is considerable scattering in the modeled backazimuth, no significant deviation drift trend is observed over time for the windless case (Fig. 8d). This indicates that global wind fields are significantly contributing to the observed backazimuth drift seen in the IMS data (Figs. 5 and 6, as well as SI2).

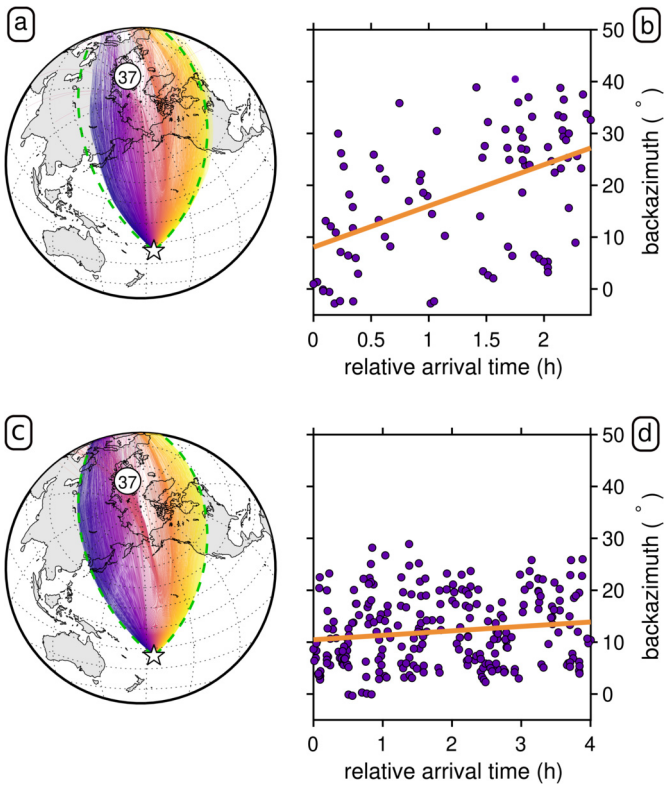

Fig. 8. Global ray-tracing through a 3D atmospheric model of winds and temperature (top row) and through the analogue model without wind (bottom row). (a, c) Global rays for a windy/windless atmosphere; (b, d) modeled relative arrival time against backazimuth calculated for the ground hits within 400 km from the station for a windy/windless atmosphere, with solid lines indicating a linear fit between time and backazimuth.

5.2. Comparisons with historical eruptions (Krakatoa, Mt. St. Helens, Pinatubo)

Based on the literature, infrasound and Lamb waves traveling around the Earth are reported for at least five VEI ≥ 5 eruptions during the last 150 yr: Krakatoa in 1883 (Simkin and Fiske, 1984), Bezymianny in 1956 (Passechnik, 1958), Mt. St. Helens in 1980 (Donn and Balachandran, 1981), El Chichón in 1982 (Mauk, 1983), and Pinatubo in 1991 (Tahira et al., 1991). However, the amplitude (700 Pa at 1,847 km) and the main period (∼2000 s) of the Lamb waves induced by the Hunga eruption significantly exceeded – up to one order of magnitude – the Lamb waves radiated from other eruptions even of larger magnitude, such as the VEI 6 Pinatubo event 1991. They are comparable only with the VEI 6 Krakatoa 1883 eruption and lead to similar yield estimates. Despite the assumption of a near-surface point source for PP71 model, the estimated order of energy magnitude found with this method (100 MT) matches the upper limit of 150 MT found by Harkrider and Press (1967) for Krakatoa with their model when trying to reproduce documented waveforms. A more jet-like source model may be required for a more in-depth investigation of the actual energy released into the atmosphere. One should also note the difference between a nuclear (instantaneous) explosion for which PP71 was tailored and the Hunga eruption which led to a longer lasting release of energy into the atmosphere, based on the SSTF and the similar duration of the infrasound signals (Fig. 4). However, and importantly, the Lamb wave train of interest seems to have been released nearly instantaneously, based on the numerous satellite observations that witnessed the event. The present yield estimate reliability within these assumptions is supported by the Lamb wave being well established and the large source-to-receiver

distance (>1,000 km). The second method based on scaling laws and nearer-field barometers backs up the first method. Estimates of 100 to 200 MT corroborate the exceptionally high explosivity of the Hunga eruption and the similarity with the 1883 Krakatoa eruption already stressed by Matoza et al. (2022).

The similar setting of Krakatoa and Hunga volcanoes, both consisting of a volcanic island partly submerged in a shallow submarine environment, suggests that phreato-magmatic processes could explain the increased explosivity of the events that is required to induce the long-period and large-amplitude Lamb waves observed for both eruptions.

In accordance with experimental observations and the Fuel-Coolant Interaction (FCI) theory, the melt interaction with water causes the formation of a vapor film that collapses and produces thermal and deformation waves in the melt resulting in its rapid brittle deformation (Morrissey et al., 2000). As a result, the fragmentation is highly increased, as suggested by the fine-grained ash production, able to feed buoyant plumes. However, the role of phreato-magmatic fragmentation for the climactic phase of Krakatoa is still debated (e.g., Madden-Nadeau et al., 2021) and for Hunga further research in this direction will require sampling of fall-out material and detailed petrological and textural analyses.

An additional similarity among the two eruptions lays in the observed eruptive sequence and the existence of a caldera. Calderas originate from subsidence or from rapid explosive ejection of material. They represent the most catastrophic geologic events affecting the Earth's surface, and it is extremely useful, and challenging, to recognize potential precursors (Lipman, 2015).

Historical descriptions of the 1883 Krakatoa eruption, as well as barometric records, demonstrate that the main event was preceded by four months of unrest that started with Vulcanian to Subplinian activity (Self, 1992) and were followed by discrete explosive events that progressively changed the island morphology (Madden-Nadeau et al., 2021). Eventually, four major explosions occurred within ~5 h leading to the caldera collapse and disruption of most of the island. This feature is argued to be a general evolution of caldera forming events and explains the explosivity in terms of magma crystallization and mixing (Madden-Nadeau et al., 2021).

Results presented in this work suggest a similar evolution. Fig. 3 shows that explosive activity at Hunga volcano started on 19 December 2021, with an initial explosive event that was recorded by 12 IMS infrasound arrays (Fig. 3a). Activity persisted for two weeks and was primarily subaerial, with infrasound persistently recorded at IS22 but with very few seismic and hydroacoustic signals detected.

On 13 January 2022, explosive activity resumed and was radiating – together with infrasound energy in the atmosphere – both seismic and hydroacoustic signals that became dominant immediately after the major event. This energy partitioning indicates a progressive deepening of the energetic source, suggesting a link between the main explosive event of 15 January, marked by the peak of the SSTF (Fig. 4), and the triggering of a caldera collapse similarly to what has been observed only for Krakatoa over the past 150 yr. Future bathymetry investigations and deposit analysis will be required to support this data-driven hypothesis.

6. Conclusions

The 15 January 2022 eruption of Hunga volcano, Tonga, generated an energetic Lamb wave and various atmospheric phenomena that were recorded on a global scale as variations of the ambient air pressure in the order of hundreds of Pa. Infrasonic, acoustic-gravity, and Lamb wave features related to the eruption were globally recorded during several circumnavigations of the globe. Infrasound arrivals have been detected after seven complete circumnavigations, more than 13 days after the blast.

Overall, the current 53 infrasound stations of the IMS network provide an excellent global capability for remote sensing of explosive and eruptive events. These are complemented in this study by other barometric as well as seismic and hydroacoustic observations together with highly efficient methods for array processing, propagation modeling, and yield estimation. A broad frequency range is analyzed to capture different acoustic-gravity wave types and to identify a suitable frequency band and uncertainty range for adapting and applying a method to estimate the eruption explosive yield.

Within this study, the volcanic eruption sequence impact on the atmospheric pressure is quantified using these global IMS infrasound observations to provide a first reliable estimate of the explosive yield of the main eruption. Consistent estimates of the magnitude order are obtained both considering PP71's work applied to Lamb waves filtered around the BV frequency and recorded within 7,000 km from the source (~100 MT), and relying on scaling relations for barometric data within a sweet spot (~200 MT). The Hunga eruption is thus among the most energetic events recorded during the last centuries and the first event ever recorded by all stations of the IMS infrasound network.

To compare the event with previous volcanic eruptions, the chronology of the Hunga volcanic activity in the weeks before the main eruption is taken into account using permanent remote infrasound observations, but also seismic and hydroacoustic sensors of the IMS network. These observations consistently describe the source characteristics in good agreement with a source time function derived from global seismometers. The Hunga eruption is most similar in intensity, yield, and eruptive behavior to the one of the Krakatoa volcano in 1883, and thus represents a unique opportunity to investigate poorly understood volcanological aspects like the phreato-magmatic interaction of large-scale eruptions, which might increase the event explosivity, as well as the identification of possible precursors leading to caldera-forming events.

Further understanding of such infrequent events with global effects will require follow-up on-site investigations of erupted material, as well as bathymetry and submerged morphology of the caldera, to be combined with multi-technology geophysical observations. Additional simulations are also needed to explain the wave propagation on a global scale, the azimuth drift observed at various stations, and the unique broadband frequency spectrum of the event.

Funding

M.A.G. was supported by the Department of Energy's National Nuclear Security Administration under Award Numbers DE-NA0003920 (MTV) and DE-NA0003921 (ETI). The views and opinions of authors expressed herein do not necessarily state or reflect those of the United States Government or any agency thereof. S.P.N. and Q.B. acknowledge partial support by the project *Middle Atmosphere Dynamics: Exploiting Infrasound Using a Multidisciplinary Approach at High Latitudes* (MADEIRA), funded by the Research Council of Norway basic research program FRIPRO/FRINATEK under Contract No. 274377.

CRediT authorship contribution statement

Conceptualization: J.V., A.L.P.; Formal analysis: J.V., P.H., C.L., M.A.G., L.C., C.P., S.P.N., Q.B., P.P., R.N., P.M.; Investigation: J.V., P.H., C.L., A.L.P., M.A.G., E.M., P.L., L.C., C.P., S.P.N., Q.B., P.P., N.S., R.N., P.M.; Methodology: J.V., P.H., C.L., M.A.G., L.C.; Validation: J.V., P.H., C.L., M.A.G., C.P.; Visualization: P.G., J.V., P.H., C.L., S.P.N., L.C.; Writing –

original draft: J.V., P.H., C.L., A.L.P., M.A.G., E.M., P.L., C.P., L.C., S.P.N., Q.B., P.P., R.N.; Writing – review & editing: all authors.

Declaration of competing interest

The authors declare no conflict of interest.

Data availability

IMS data are available from the CTBTO Preparatory Commission for scientific purposes through the virtual Data Exploitation Centre (vDEC): https://www.ctbto.org/specials/vdec/. Other barometer data used for estimating the yield (station and network names are mentioned in Section 4.3) are available through IRIS (http://www.iris.edu). ECMWF products, including the atmospheric high-resolution model analysis, are partly available via www.ecmwf.int/en/forecasts/accessing-forecasts under CC BY 4.0 License, or via the ECMWF MARS system for users within ECMWF Member and Co-operating States. The Bulletin of the International Seismological Centre (https://doi.org/10.31905/D808B830) includes events listed in the REB of the IDC.

Acknowledgements

The authors are grateful to Elizabeth A. Silber and Eric Dunham for their valuable reviews. All authors thank the CTBTO and the IMS station operators for guaranteeing the high quality of the infrasound and hydroacoustic data. Authors also thank R. Greenwood from Tsunami Technical Lead Marine and Antarctic Environment Prediction Service Bureau of Meteorology (Melbourne) for providing Nukua'lofa barometric data with the assistance of the Tongan Meteorological office technical staff which fixed the communication issues after the eruption. M.A. Garcés is grateful to M. Colet and B. Williams for data wrangling, and to B. Shiro for helping navigate through the IRIS holdings. K. Takazawa, P. Brown, and K. Kim provided valuable consultations on yield-scaling relations. C. Listowski and A. Le Pichon thank N. Lardjane for fruitful discussions. The views expressed herein are those of the authors and not necessarily reflect the views of the CTBTO Preparatory Commission.

Appendix A. Supplementary material

Supplementary material related to this article can be found online at https://doi.org/10.1016/j.epsl.2022.117639.

References

Andrews, R.G., 2022. Tonga shock wave created tsunamis in two different oceans. Sci. News. https://doi.org/10.1126/science.ada0562. Published 25 January 2022.

Beyreuther, M., Barsch, R., Krischer, L., Megies, T., Behr, Y., Wassermann, J., 2010. ObsPy: a Python toolbox for seismology. Seismol. Res. Lett. 81, 530–533. https://doi.org/10.1785/gssrl.81.3.530.

Blom, P.S., Waxler, R., 2017. Modeling the refraction of microbaroms by the winds of a large maritime storm. J. Acoust. Soc. Am. 142, 3520–3529. https://doi.org/10.1121/1.5016809.

Blom, P., 2019. Modeling infrasonic propagation through a spherical atmospheric layer—analysis of the stratospheric pair. J. Acoust. Soc. Am. 145 (4), 2198–2208. https://doi.org/10.1121/1.5096855.

Bretherton, F.P., 1969. Lamb waves in a nearly isothermal atmosphere. Q. J. R. Meteorol. Soc. 95, 754–757. https://doi.org/10.1002/qj.49709540608.

Cansi, Y., 1995. An automatic seismic event processing for detection and location: the P.M.C.C method. Geophys. Res. Lett. 22 (9), 1021–1024. https://doi.org/10.1029/95GL00468.

Červený, V., Soares, J.E.P., 1992. Fresnel volume ray tracing. Geophysics 57 (7), 902–915. https://doi.org/10.1190/1.1443303.

Cronin, S.J., Brenna, M., Smith, I.E.M., Barker, S.J., Tost, M., Ford, M., Tonga'onevai, S., Kula, T., Vaiomoung, R., 2017. New volcanic island unveils explosive past. Eos 98. https://doi.org/10.1029/2017EO076589.

Donn, W.L., Balachandran, N.K., 1981. Mount St. Helens eruption of 18 May 1980: air waves and explosive Yield. Nature 213, 539–541. https://doi.org/10.1126/science.213.4507.539.

Drob, D.P., Emmert, J.T., Meriwether, J.W., Makela, J.J., Doornbos, E., Conde, M., Hernandez, G., Notos, J., Zawdie, K.A., McDonald, S.E., Huba, J.D., Klenzing, J.H., 2015. An update to the Horizontal Wind Model (HWM): the quiet time thermosphere. Earth Space Sci. 2, 301–319. https://doi.org/10.1002/2014EA000089.

Dziewonski, A.M., Anderson, D.L., 1981. Preliminary reference Earth model. Phys. Earth Planet. Inter. 25 (4), 297–356. https://doi.org/10.1016/0031-9201(81)90046-7.

Ekström, G., 2011. A global model of Love and Rayleigh surface wave dispersion and anisotropy, 25-250 s. Geophys. J. Int. 187 (3), 1668–1686. https://doi.org/10.1111/j.1365-246X.2011.05225.x.

Francis, S.H., 1973. Acoustic-gravity modes and large-scale traveling ionospheric disturbances of a realistic, dissipative atmosphere. J. Geophys. Res. 78 (13), 2278–2301. https://doi.org/10.1029/JA078i013p02278.

Garcés, M.A., Fee, D., Matoza, R., 2013. Volcano acoustics. In: Fagents, S.A., Lopes, R.M.C., Gregg, T.K.P. (Eds.), Modeling Volcanic Processes: The Physics and Mathematics of Volcanism. Cambridge University Press.

Garcés, M.A., 2019. Explosion source models. In: Le Pichon, A., Blanc, E., Hauchecorne, A. (Eds.), Infrasound Monitoring for Atmospheric Studies, second edition. Springer, Switzerland, pp. 273–345.

Global Volcanism Program, 2022. Report on Hunga Tonga-Hunga Ha'apai (Tonga). In: Sennert, S.K. (Ed.), Weekly Volcanic Activity Report, 16 February–22 February 2022. Smithsonian Institution and US Geological Survey.

Gossard, E.E., Hooke, W.H., 1975. Waves in the Atmosphere. Elsevier Scientific Publishing Co., Amsterdam, Oxford, New York.

Green, D.N., Bowers, D., 2010. Estimating the detection capability of the International Monitoring System infrasound network. J. Geophys. Res. 115, D18116. https://doi.org/10.1029/2010JD014017.

Harkrider, D., Press, F., 1967. The Krakatoa air-sea waves: an example of pulse propagation in coupled systems. Geophys. J. R. Astron. Soc. 13, 149–159. https://doi.org/10.1111/j.1365-246X.1967.tb02150.x.

Hupe, P., Ceranna, L., Le Pichon, A., Matoza, R.S., Mialle, P., 2022. International Monitoring System infrasound data products for atmospheric studies and civilian applications. Earth Syst. Sci. Data Discuss. https://doi.org/10.5194/essd-2021-441, submitted for publication.

Kanamori, H., Given, J.W., 1982. Analysis of long-period seismic waves excited by the May 18, 1980, eruption of Mount St. Helens—a terrestrial monopole? J. Geophys. Res., Solid Earth 87 (B7), 5422–5432. https://doi.org/10.1029/JB087iB07p05422.

Kim, K., Rodgers, A.R., Garcés, M.A., Myers, S.C., 2021. Empirical acoustic source model for chemical explosions in air. Bull. Seismol. Soc. Am. 111, 2862–2880. https://doi.org/10.1785/0120210030.

Kshevetskii, S.P., Kurdyaeva, Y.A., Gavrilov, N.M., 2021. Spectra of acoustic-gravity waves in the atmosphere with a quasi-isothermal upper layer. Atmosphere 12, 818. https://doi.org/10.3390/atmos12070818.

Lamb, H., 1932. Hydrodynamics. Cambridge University Press, New York. Reprinted in 1995.

Le Pichon, A., Ceranna, L., Pilger, C., Mialle, P., Brown, D., Herry, P., Brachet, N., 2013. The 2013 Russian fireball largest ever detected by CTBTO infrasound sensors. Geophys. Res. Lett. 40, 3732–3737. https://doi.org/10.1002/grl.50619.

Lindzen, R.S., Blake, D., 1972. Lamb waves in the presence of realistic distributions of temperature and dissipation. J. Geophys. Res. 77 (12), 2166–2176. https://doi.org/10.1029/JC077i012p02166.

Lipman, P.W., 2015. Calderas. In: Sigurdsson, H., McNutt, S., Rymer, H., Stix, J. (Eds.), Encyclopedia of Volcanoes, 2nd edition. Academic Press, London, pp. 643–662.

Madden-Nadeau, A.L., Cassidy, M., Pyle, D.M., Mather, T.A., Watt, S.F.L., Engwell, S.L., Abdurrachman, M., Nurshal, M.E.M., Tappin, D.R., Ismail, T., 2021. The magmatic and eruptive evolution of the 1883 caldera-forming eruption of Krakatau: integrated field- to crystal-scale observations. J. Volcanol. Geotherm. Res. 411, 107176. https://doi.org/10.1016/j.jvolgeores.2021.107176.

Marty, J., Doury, B., Kramer, A., 2021. Low and high broadband spectral models of atmospheric pressure fluctuation. J. Atmos. Ocean. Technol. 38 (10), 1813–1822. https://doi.org/10.1175/JTECH-D-21-0006.1.

Matoza, R.S., Fee, D., Assink, J.D., Iezzi, A.M., Green, D.N., Kim, K., Toney, L., Lecocq, T., Krishnamoorthy, S., Lalande, J.-M., Nishida, K., Gee, K.L., Haney, M.M., Ortiz, H.D., Brissaud, Q., Martire, L., Rolland, L., Vergados, P., Nippress, A., Park, J., Shani-Kadmiel, S., Witsil, A., Arrowsmith, S., Caudron, C., Watada, S., Perttu, A.B., Taisne, B., Mialle, P., Le Pichon, A., Vergoz, J., Hupe, P., Blom, P.S., Waxler, R., De Angelis, S., Snively, J.B., Ringler, A.T., Anthony, R.E., Jolly, A.D., Kilgour, G., Averbuch, G., Ripepe, M., Ichihara, M., Arciniega-Ceballos, A., Astafyeva, E., Ceranna, L., Cevuard, S., Che, I.-Y., De Negri, R., Ebeling, C.W., Evers, L.G., Franco-Marin, L.E., Gabrielson, T.B., Hafner, K., Harrison, R.G., Komjathy, A., Lacanna, G., Lyons, J., Macpherson, K.A., Marchetti, E., McKee, K.F., Mellors, R.J., Mendo-Pérez, G., Mikesell, T.D., Munaibari, E., Oyola-Merced, M., Park, I., Pilger, C., Ramos, C., Ruiz, M.C., Sabatini, R., Schwaiger, H.F., Tailpied, D., Talmadge, C., Vidot, J., Webster, J., Wilson, D.C., 2022. Atmospheric waves and global seismoacoustic observations of the January 2022 Hunga eruption, Tonga. Science. https://doi.org/10.1126/science.abo7063, published online 12 May 2022.

Mauk, F.J., 1983. Utilization of seismically recorded infrasonic-acoustic signals to monitor volcanic explosions: the El Chichón sequence 1982 – a case study. J. Geophys. Res. 88, 10385–10401. https://doi.org/10.1029/JB088iB12p10385.

Mialle, P., Brown, D., Arora, N., 2019. Advances in operational processing at the International Data Centre. In: Le Pichon, A., Blanc, E., Hauchecorne, A. (Eds.), Infrasound Monitoring for Atmospheric Studies – Challenges in Middle-Atmosphere Dynamics and Societal Benefits. Springer, pp. 209–248.

Morrissey, M., Zimanowski, B., Wohletz, K., Buettner, R., 2000. Phreatomagmatic fragmentation. In: Sigurdsson, H., McNutt, S., Rymer, H., Stix, J. (Eds.), Encyclopedia of Volcanoes, 1st edition. Academic Press, London, pp. 431–445.

Nishida, K., Kobayashi, N., Fukao, Y., 2014. Background Lamb waves in the Earth's atmosphere. Geophys. J. Int. 196 (1), 312–316. https://doi.org/10.1093/gji/ggt41.

Passechnik, I.P., 1958. Seismic and air waves which arose during an eruption of the Volcano Bezymyanny, on March 30, 1956. Izv. Geophys. Ser., 1121–1126 (English translation by A.S. Ryall.).

Picone, J.M., Hedin, A.E., Drob, D.P., Aikin, A.C., 2002. NRLMSISE-00 empirical model of the atmosphere: statistical comparisons and scientific issues. J. Geophys. Res. Space Phys. 107 (A12). https://doi.org/10.1029/2002JA009430. SIA-15.

Pierce, A., Posey, J., 1971. Theory of the excitation and propagation of Lamb's atmospheric edge mode from nuclear explosions. Geophys. J. Int. 26 (1–4), 341–368. https://doi.org/10.1111/j.1365-246X.1971.tb03406.x.

Pilger, C., Hupe, P., Gaebler, P., Ceranna, L., 2021. 1001 rocket launches for space missions and their infrasonic signature. Geophys. Res. Lett. 48, e2020GL092262. https://doi.org/10.1029/2020GL092262.

Poli, P., Shapiro, N., 2022. Rapid characterization of large volcanic eruptions: measuring the impulse of the Hunga Tonga explosion from teleseismic waves. Geophys. Res. Lett. 49, e2022GL098123. https://doi.org/10.1029/2022GL098123.

Press, F., Harkrider, D., 1962. Propagation of acoustic-gravity waves in the atmosphere. J. Geophys. Res. 67 (10), 3889–3908. https://doi.org/10.1029/JZ067i010p03889.

Schnurr, J.M., Kim, K., Garcés, M.A., Rodgers, A., 2020. Improved parametric models for explosion pressure signals derived from large datasets. Seismol. Res. Lett. 91, 1752–1762. https://doi.org/10.1785/0220190278.

Self, S., 1992. Krakatau revisited: the course of events and interpretation of the 1883 eruption. GeoJournal 28 (2), 109–121. https://doi.org/10.1007/BF00177223.

Sigl, M., Winstrup, M., McConnell, J., et al., 2015. Timing and climate forcing of volcanic eruptions for the past 2,500 years. Nature 523, 543–549. https://doi.org/10.1038/nature14565.

Simkin, T., Fiske, R.S., 1984. Krakatau 1883: The Volcanic Eruption and Its Effects. Smithsonian Institution Press, Washington. 464 pp.

Stevens, J.L., Divnov, I.I., Adams, D.A., Murphy, J.R., Bourchik, V.N., 2002. Constraints on infrasound scaling and attenuation relations from Soviet Explosion Data. In: Der, Z.A., Shumway, R.H., Herrin, E.T. (Eds.), Monitoring the Comprehensive Nuclear-Test-Ban Treaty: Data Processing and Infrasound. Pageoph Topical Volumes. Birkhäuser, Basel.

Stockwell, R.G., Mansinha, L., Lowe, R.P., 1996. Localization of the complex spectrum: the S transform. IEEE Trans. Signal Process. 44 (4), 998–1001. https://doi.org/10.1109/2F78.492555.

Tahira, M., Nomura, M., Sawada, Y., Kamo, K., 1991. Infrasonic and acoustic-gravity waves generated by the Mount Pinatubo eruption of June 15, 1991. In: Fire and Mud: Eruptions and Lahars of Mount Pinatubo, Philippines, pp. 601–614. https://pubs.usgs.gov/pinatubo/tahira/, 1996.

Vaughan, R.G., Webley, P.W., 2010. Satellite observations of a surtseyan eruption: Hunga Ha'apai Tonga. J. Volcanol. Geotherm. Res. 198, 177–186. https://doi.org/10.1016/j.jvolgeores.2010.08.017.

Vergoz, J., Le Pichon, A., Millet, C., 2019. The antares explosion observed by the USArray: an unprecedented collection of infrasound phases recorded from the same event. In: Le Pichon, A., Blanc, E., Hauchecorne, A. (Eds.), Infrasound Monitoring for Atmospheric Studies – Challenges in Middle-Atmosphere Dynamics and Societal Benefits. Springer, pp. 471–482.

Walker, K.T., Hedlin, M.A.H., 2010. A review of wind-noise reduction methodologies. In: Le Pichon, A., Blanc, E., Hauchecorne, A. (Eds.), Infrasound Monitoring for Atmospheric Studies. Springer, pp. 141–182.

Patrick Hupe is a PostDoc (since 2019) at the Federal Institute for Geosciences and Natural Resources (BGR) in Hannover within the sub-department Federal Seismological Survey / Nuclear-Test Ban (B4.3). He earned his PhD in Atmospheric Physics from Ludwig-Maximilians-Universität in Munich in 2019. As a PhD candidate, he worked within the project "Atmospheric Dynamics Research InfraStructure in Europe" (ARISE, 2015–2018) at BGR. His current research activities at BGR include the global characterization of ambient infrasound and CTBT analyses, the investigation of acoustic wave propagation and atmospheric dynamics, and the detection and characterization of infrasonic and seismoacoustic events such as explosions, volcanic eruptions and meteoroids.